

1 This is a non-peer reviewed preprint submitted to EarthArXiv.

2

3 This manuscript is in review at Advances in Water Resources.

4

5 Menke, H.P.^{1,2} (h.menke@hw.ac.uk)

6 Gao, Y.² (y.gao15@imperial.ac.uk)

7 Linden, S.³ (sven.linden@math2market.de)

8 Andrew, M.G.⁴ (matthew.andrew@zeiss.com)

9

10 ¹Institute of Petroleum Engineering, Heriot-Watt University, Edinburgh, UK

11 ²Qatar Carbonates and Carbon Storage Research Centre, Imperial College London, UK

12 ³Math2Market GeoDict, Kaiserlautern, Germany

13 ⁴Zeiss Microscopy, Pleasanton, CA, USA

14

15 TITLE

16

17 **Using nano-XRM and high-contrast imaging to inform micro-porosity permeability**
18 **during Stokes-Brinkman single and two-phase flow simulations on micro-CT images.**

19

20 Menke, H.P.^{1,2}; Gao, Y.²; Linden, S.³; Andrew, M.G.⁴

21

22 ¹Institute of Petroleum Engineering, Heriot-Watt University, Edinburgh, UK

23 ²Qatar Carbonates and Carbon Storage Research Centre, Imperial College London, UK

24 ³Math2Market GeoDict, Kaiserslautern, Germany

25 ⁴Zeiss Microscopy, Pleasanton, CA, USA

26

27 TITLE

28

29 **Using nano-XRM and high-contrast imaging to inform micro-porosity permeability**
30 **during Stokes-Brinkman single and two-phase flow simulations on micro-CT images.**

31

32 ABSTRACT

33

34 Carbonate rocks have particularly complex and multiscale pore systems which are weakly
35 understood. In this study we use combined experimental, modelling, and pore space generation
36 methods to tackle the impact of micro-porosity on the bulk flow properties of Estailades
37 limestone. First, a nano-core from a microporous grain of Estailades Limestone was scanned
38 using x-ray nano tomography (nano-XRM). The information from the nano-XRM scan was
39 then used as input into an object-based pore network generator, on which permeability fields
40 were simulated for a range of porosities, creating a synthetic Kozeny-Carman porosity-
41 permeability relationship targeted for the specific micro porous system present in
42 Estailades. We found a good match between experimental and simulated Mercury Intrusion
43 Capillary Pressure (MICP) range in the imaged geometry and a good match between the
44 imaged and object generated permeabilities and MICP.

45 A micro-core of Estailades was then scanned using x-ray microtomography (μ CT), the
46 differential pressure was measured during single phase flow, and the rock was flooded with
47 highly doped brine to differentiate connected from unconnected micro-porosity. The
48 differential contrast between the dry and doped images was used to assign a porosity to each
49 voxel of connected micro-porosity. The flow through the pore space was then solved using a
50 Stokes-Brinkman solver while a second segmented image with no micro-porosity was solved
51 a Stokes solver. The differences between the measured permeability and the two computed
52 permeabilities was evaluated. We found that there was good agreement between both the
53 computed permeability of the Stokes and Stokes-Brinkman simulation with the measured
54 permeability. However, there was considerable differences in the velocity fields with the
55 Stokes-Brinkman simulation capturing stagnant regions of the pore space that were not present
56 in the Stokes simulations.

57 Additionally, we investigated the implications of including micro-porosity in
58 estimations of relative permeability. Nitrogen was experimentally co-injected through the core
59 with doped brine at a 50% fractional flow and imaged to the two-phase effective permeability.
60 This experimental measurement was compared with the numerical permeability simulated
61 using both Stokes and Stokes-Brinkman models for several saturation points along a synthetic
62 MICP injection curve. We found that the Stokes simulation was not able to predict relative
63 permeability with this method due to the major flow paths in the macro-porosity being impeded
64 by the injected non-wetting phase. The Stokes-Brinkman simulations, however, allowed flow
65 in the microporous regions around these blocked flow paths and was able to achieve a relative
66 permeability prediction that was a reasonable match to the experimental measurement. This
67 method could be used to predict relative permeability in water wet pore-structures with high
68 micro-porosity.

69

70

71 INTRODUCTION

72

73 Experiments combining X-ray microtomography (μ CT) with *in situ* flow apparatus is now an
74 accepted method of studying pore scale processes in real rocks [1, 2]. Pore-scale imaging
75 experiments coupled with simulation is an increasingly important tool used in industry prediction
76 of geological and petrophysical properties including porosity and connectivity [3],
77 mineralogical heterogeneity [4], and relative permeability [5, 6].

78

79 Typically, these simulations are done on the segmented image and are only concerned with the
80 macro pore space where the fluid solid boundary is fully resolved and able to be segmented
81 into pore and grain on a voxel-by-voxel basis [7]. When the rock grains are solid and the pore
82 throats are large compared to the image resolution, a reasonably accurate segmentation is all
83 that is needed to get a realistic estimation of flow through the rock [8, 9]. However, not all
84 grains are non-porous, and intra-granular micro-porosity is a significant contributor to total
85 carbonate micro-porosity [10]. Most carbonate rocks have grains that are micro-porous [11] –
86 hereafter defined as a grain that has interior porosity that is not fully resolvable at the resolution
87 of the imaging apparatus. Furthermore, over 50% of world oil is stored in carbonate reservoirs
88 [12].

89

90 The Stokes-Brinkman flow simulation technique combines Darcy's law effective media flow
91 with pore-scale Stokes flow has been proposed as a solution to this problem bridging the gap
92 between the fully resolved pore-scale and the partially resolved nano-scale [13, 14],
93 particularly when macro and micro-porosity are effectively separated in spatial length scale. In
94 many variations of Stokes-Brinkman simulations Darcy's law is solved in the semi-solid rock
95 matrix based on an estimated permeability which is derived from the calculated porosity using
96 the relative greyscale between solid grains and pore space.

97

98 Assigning porosity values to partially resolved voxels is well documented [15] and has been
99 used in conjunction with Mercury Intrusion Capillary Pressure (MICP) measurements in many
100 core-scale simulations on x-ray tomography images that do not have sufficient resolution to
101 see the structure and connectivity of the pore space needed to make a Navier-Stokes calculation
102 possible. In this case, reconstructed greyscale values are used as an analogue for porosity and
103 the permeability is assigned to each porosity value based on Kozeny-Carman estimations. This
104 method of assigning a relationship between porosity and permeability, however, is based on an
105 even the assumption that the porous medium is effectively represented by an even packing of
106 equally-sized elliptical beads [16, 17]. Furthermore, this method does not include any influence
107 associated with micro-pore space connectivity [18]. A section of micro-porosity may have high
108 porosity without necessarily being connected to the macro porosity in any significant way.

109

110 To quantify the connected porosity of the pore space Lin, Al-Khulaifi [19] flooded the rock
111 with highly doped brine at varying concentrations. They found that the highest doped brine
112 gave the best contrast and was able to quantify the distribution of connected and unconnected
113 porosity, as well as the porosity distribution of the connected porosity by thresholding the
114 difference between the dry scan and the doped scan. Any differences between the two images
115 must be associated with a change in saturation of the micro-porosity, with the magnitude of the
116 change being associated with the fractional change. This is similar to the method used by Ott,
117 Andrew [20] to quantify pore scale behaviour during salt precipitation.

118

119 The Kozeny-Carman equation related the permeability K to the porosity ϕ by:

120

$$K = \frac{\varphi^3}{c(1 - \varphi)^2 S^2}$$

121

where c is the Kozeny constant and S is the specific surface area based on the solid volume.

122

This relationship can be used to relate local pore structure to macroscopic flow behaviour;

123

however, the Kozeny-Carman method is fundamentally flawed when representing more

124

complex pore structures as it assumes a homogeneous pore structure of evenly packed,

125

uniformly sized spherical grains. Furthermore, the Kozeny-Carman method does not

126

incorporate any geological processes that would change the shape and connectivity of the

127

pore space (i.e. compaction and diagenesis). To properly define this relationship at the pore -

128

scale it is necessary to image the structure of the micro-porosity and numerically calculate the

129

porosity and permeability relationship from a segmented image which well resolves the pore

130

structure at the nano-scale.

131

Nano-scale techniques including FIB-SEM (focused ion beam scanning electron microscopy),

132

helium ion microscopy, and nano x-ray microscopy (nano-XRM) have emerged as

133

technologies capable of resolving this porosity at the resolution of several nm for FIB-SEM

134

and nano-XRM [21] down to tens of angstroms for the helium ion [22, 23]. However, when

135

imaging at this resolution it is only possible to see small volumes of rock on the order around

136

$10 \mu\text{m} \times 10 \mu\text{m} \times 10 \mu\text{m}$ for charged beam instruments and around $65 \mu\text{m} \times 65 \mu\text{m} \times 65 \mu\text{m}$ for

137

nano-XRM. Thus, it is necessary to either image many different parts of the micro pore

138

structure or to find a way of extrapolating these structures synthetically.

139

140

Early digital rock analysis efforts used synthetic pore space generation extensively to examine

141

simple systems at the pore scale, however as imaging technologies have improved, it has

142

largely supplanted synthetic pore network generation for the examination of simple geometries.

143

Nevertheless, synthetic techniques do present specific advantages, especially when examining

144

mechanisms behind various processes while controlling the amount of heterogeneity [24, 25]

145

These synthetic pore spaces can either be constructed physically, usually by glass beads or

146

etchings in glass (e.g. [26-28]) or numerically using a pore space generator, using stochastic or

147

object-based techniques, subject to various constraints (e.g. [29]).

148

149

Recently, Andrew [30] has used a combination of numerical pore space generation and

150

multiscale imaging to investigate the porosity-permeability relationships of shale and

151

sandstones. He found that the (geological) diagenetic processes inherent in the creation of the

152

porosity should dictate how to approach the generation so as to accurately predict the evolution

153

of permeability. Shales have a porosity defined by authigenic growth within a deformable

154

matrix, making the pore structure significantly more spherical than intergranular pore

155

structures, common in sandstones and carbonates. As such, authigenic organic hosted pore

156

networks can be modelled (to a high level of statistical similarity when compared with imaged

157

pore networks) using a network of (overlapping) spherical pores, while sandstones can be

158

modelled similarly accurately by modelling individual grains as convex polyhedra, with the

159

pore network given by the space between the grains.

160

161

The goal of this study is to present a method that combines fluid flow experiments with

162

multiscale imaging of macro and micro-porosity and synthetic pore space generation to

163

increase the accuracy of numerical multiphase pore-scale simulations on microporous rocks

164

using Stokes-Brinkman simulations.

165

166 First, we imaged the micro-porosity of Estailades limestone using nano-XRM at a spatial
167 resolution of 50nm. We then analysed this image to generate a statistical description of the
168 micritic grains which constitute the nano-porous network. This statistical description was then
169 used to generate a range of pore networks using object-based techniques, creating a porosity-
170 permeability map specific to this rock type. A 6-mm diameter, 24-mm long core plug of
171 Estailades Limestone was then imaged using micro-CT at a resolution of 3.9 μm , with and
172 without high contrast brine. This was then segmented into pore, grain, and 12 microporous
173 regions of varying porosity, which was used as the input to a Stokes-Brinkman solver with
174 each of the microporous regions assigned a permeability based on the generated porosity-
175 permeability relationship. The permeability and flow fields of the Stokes-Brinkman simulation
176 were then compared to a Stokes only flow simulation with the same pore space.

177

178 We then ran a steady-state flow experiment on the same core *in situ*. Nitrogen gas and 30 wt.
179 % potassium iodide (KI) brine were injected into the core at a fractional flow of 0.5 and allowed
180 to come to steady-state. The core was then imaged, and the differential pressure was measured,
181 corresponding to a single point on the relative permeability curve. Concurrently, relative
182 permeability was simulated with GeoDict software [31] by using an MICP-like simulated
183 injection method where the non-wetting phase is allowed to occupy regions of the pore network
184 using a maximal inscribed spheres technique. Permeability through only the wetting phase was
185 then simulated using both Stokes and Stokes-Brinkman methods by simulating single phase
186 flow through the wetting phase only. The relative permeability measured *in situ* was then
187 compared to these simulation results.

188

189 MATERIALS AND METHODS

190

191 **Sample Characterisation**

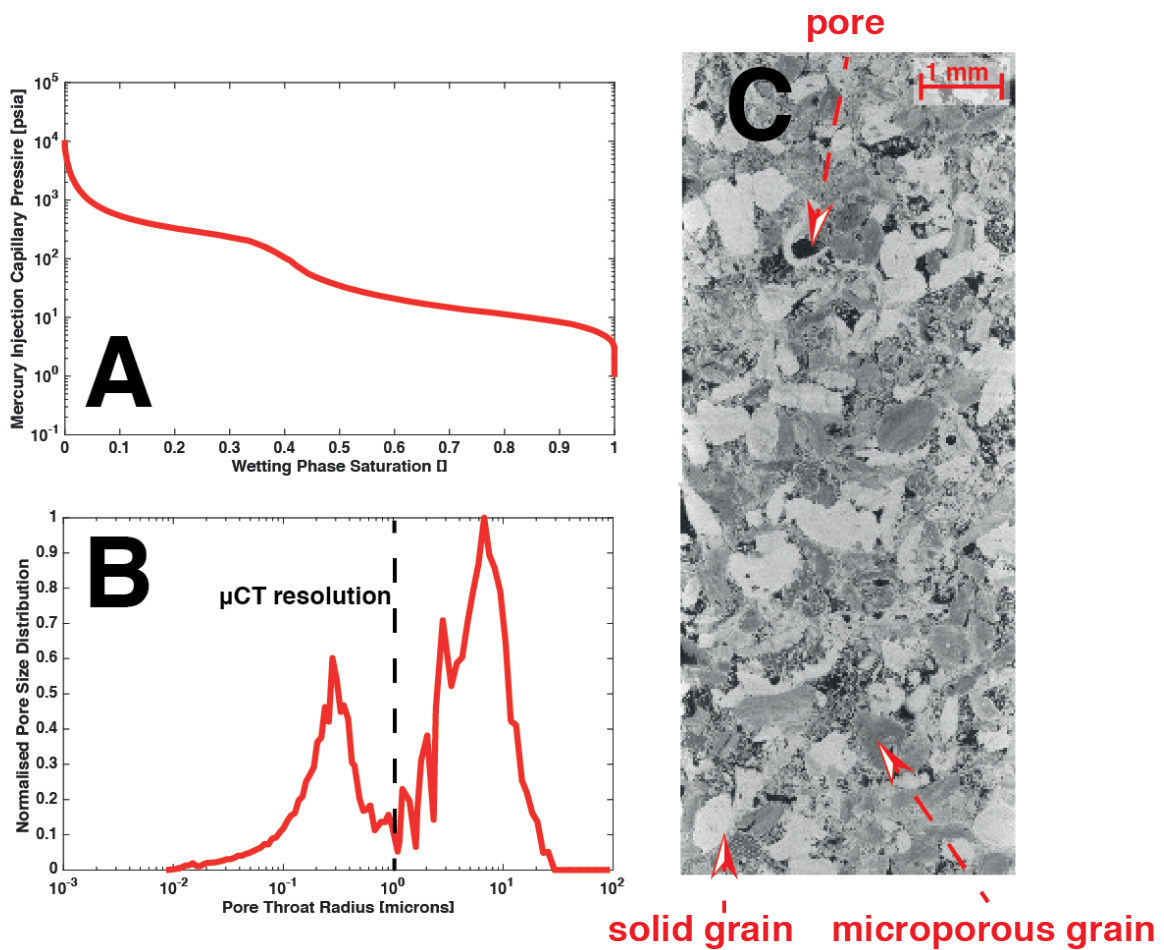
192

193 Estailades is a limestone quarried at Oppede, France. It was deposited 22 million years ago
194 and is composed of mostly calcite (>97%) with a minor quartz component. Estailades is a
195 medium to coarse-grained bioclastic grainstone with microporous bioclast grains. The helium
196 porosity is 0.295 and a bulk-scale absolute permeability of $1.490 \times 10^{-12} \text{ m}^2$ (measured at
197 Weatherford Laboratories, East Grinstead, UK).

198

199 Estailades is a well-connected heterogeneous carbonate. The MICP curve and pore-throat
200 distribution show a clear bimodal population of pore throats [Figure 1]. However, only the
201 larger population of throats is accessible to μ -CT imaging, and only contributes around half of
202 the total porosity, with the remainder residing in the microporous bioclasts.

203

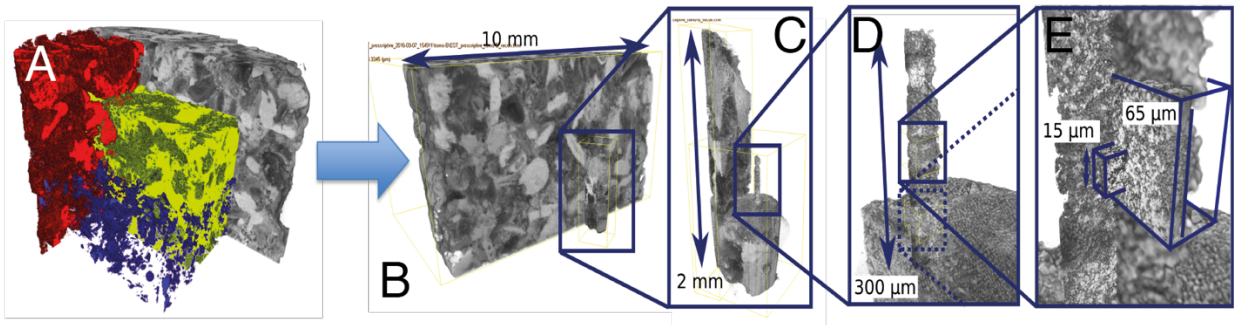


204
 205
 206
 207
 208
 209
 210
 211
 212
 213
 214
 215
 216
 217
 218

Figure 1 Estailades limestone MICP curves (A,B) with the μ CT resolution shown as a dashed black line. A μ CT image (C) with labelled pores, solid, and microporous grains.

Nano scale Imaging

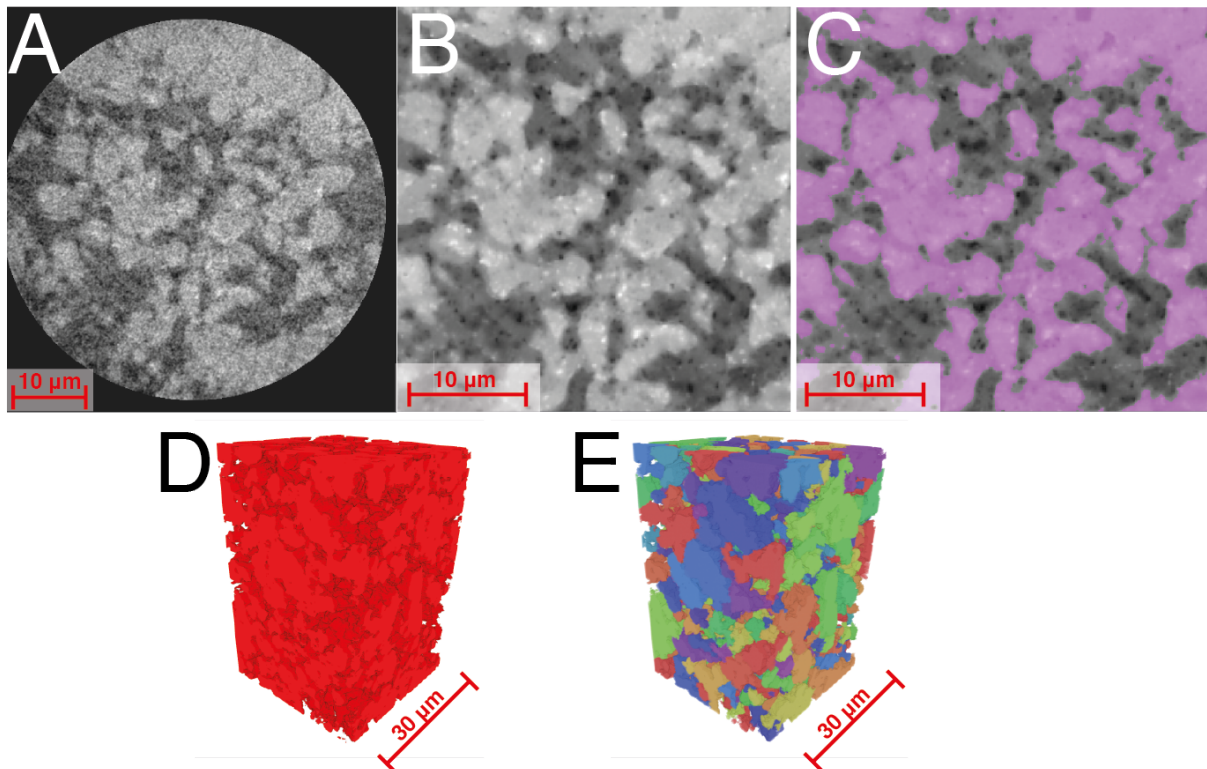
The ZEISS Xradia Ultra 810 nano-XRM was used to image microporous structure down to a resolution of 50 nm [Figure 2]. The extremely high resolution of this system requires relatively stringent sample size restrictions, with samples having a diameter no larger than 100 μ m. Sample preparation of such a small sample is extremely challenging, even in non-heterogeneous samples, and the heterogeneous nature of many geological systems compounds this challenge significantly. To prepare such samples a complex multi-stage sample preparation protocol was performed using an Oxford gimballed laser micro-machining mill model A-532-DW (www.oxfordlasers.com) [32].



219 **Figure 2** A core of Estailades is scanned in the μ CT (A) and the pores (red), solid grains (blue),
 220 and microporous grains (yellow) are identified. An interesting subsection is identified (B) and
 221 milled (C). A section of the milled section (D) is then scanned in the nano-XRM (E).
 222
 223

224 First a 10mm diameter mechanically drilled sample of (air saturated) Estailades was scanned
 225 low (10 μ m) resolution using a ZEISS XRM-510 μ CT. Fiducial marks made of aluminum tape
 226 were placed on the surface of the sample to enable alignment between the laser micro-
 227 machining stage and the sample. The low-resolution image was then segmented into micro-
 228 porosity, macro-porosity and solid mineral grains using ZEISS Zen Intellesis machine learning
 229 based segmentation [Figure 3]. As Estailades is very simple mineralogically (>97% calcite),
 230 the greyscale of each voxel within the micro-porosity is only associated with the internal
 231 porosity of that voxel, ranging from the value observed within the macro-porosity
 232 (corresponding to a 100% porosity within the voxel) to that observed within the solid grain
 233 (corresponding to a 0% porosity). The greyscale distribution within the microporous phase
 234 therefore corresponds to its internal porosity distribution [Figure 3]. A 30 μ m \times 30 μ m \times 30
 235 μ m region of micro-porosity (corresponding to 3 \times 3 \times 3 voxels within the macroscopic image)
 236 was then identified which corresponded to the modal porosity within the porosity distribution
 237 of the micro-porosity (a porosity of 40%). The offset of this region relative to the sample
 238 fiducial marks was then measured, and the region of interest (ROI) aligned underneath the laser
 239 axis. A coarse pillar of dimensions 800 μ m diameter, 2 mm length was extracted from the
 240 sample using the laser micro-machining in a top-down fashion. This sample was then
 241 transferred to the end of a dowel pin using an automated sample transfer procedure. This coarse
 242 pillar was then imaged within the μ CT with a voxel size of 800 nm along its length. This image
 243 was then registered with the macroscopic (10 μ m voxel size) image of the 10mm diameter
 244 pillar using a normalized mutual information metric.
 245

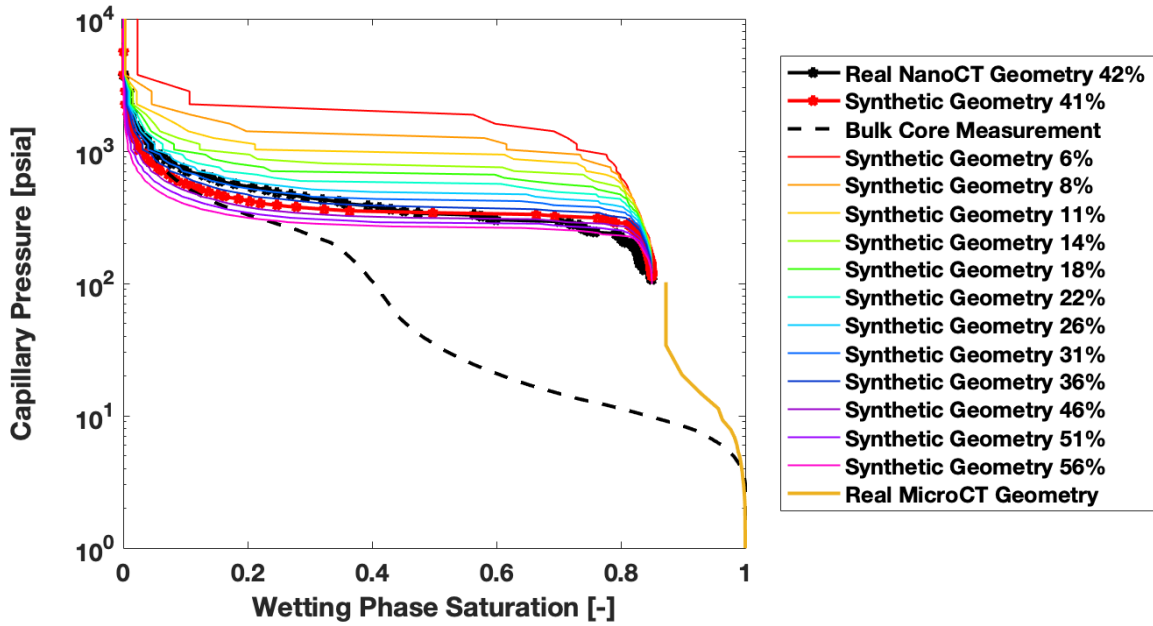
246 The coarse pillar was then transferred to a rotational stage within the laser system with a
 247 rotational axis perpendicular to the laser axis. The sample was then slowly reduced to produce
 248 a fine pillar 65 μ m in diameter operating the laser in lathe-like fashion. This pillar was then
 249 imaged along its length within the ZEISS Ultra NanoCT at low resolution (128nm voxel size).
 250 This dataset was then registered with the lower resolution dataset of the coarse (800 μ m
 251 diameter) pillar (and thereby the macroscopic image of the 10mm diameter core). This multi-
 252 scale representation of the micro-porosity was then inspected to identify the location within the
 253 nano-XRM corresponding to location within the fine pillar of the region of modal (40%)
 254 porosity, initially identified from the macroscopic image. This region was then scanned at the
 255 final, highest resolution (32nm voxel size) non-invasively within the fine pillar. The internal
 256 structure of the imaged micro-porosity consists of subhedral crystals of micrite, consistent with
 257 SEM and transmitted light microscopy analysis of this sample [33].
 258
 259



260
 261 **Figure 3** (A) The raw nano-XRM image, (B) cropped and filtered image, (C) grains identified
 262 by machine learning, (D) segmented 3-D image, and (E) separated grains.
 263

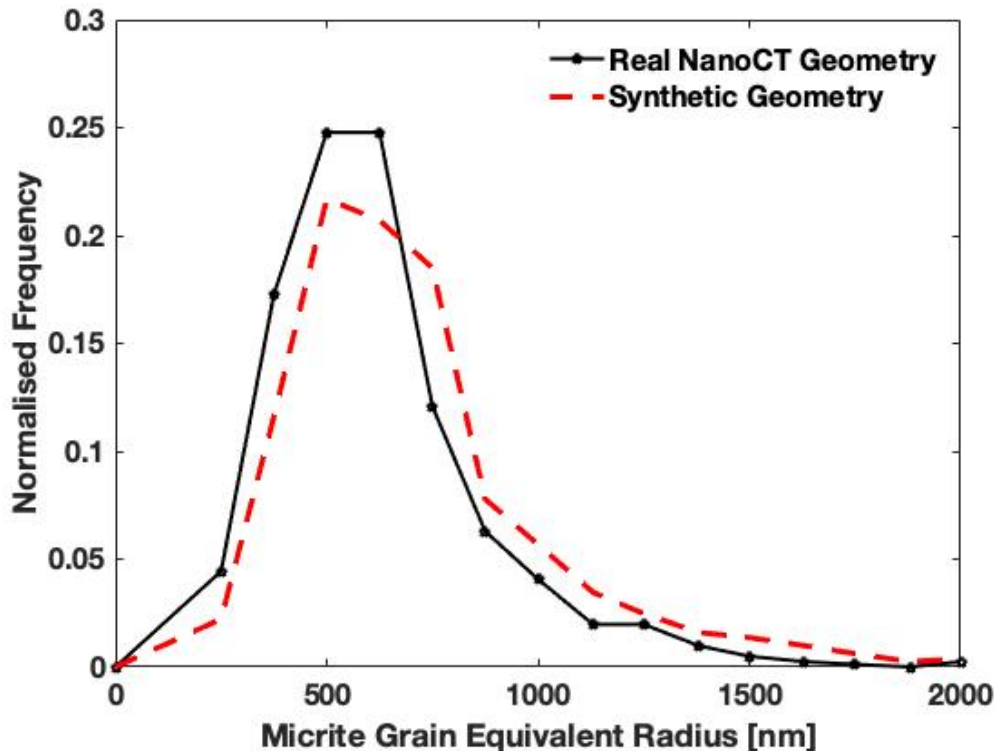
264 The resulting reconstructed image was first denoised using an edge preserving non-local means
 265 filter, then segmented using ZEISS Zen Intellesis machine learning based segmentation. Such
 266 a segmentation technique has been showed in quantitative benchmarks to be significantly more
 267 robust when dealing with such noisy and challenging images [34, 35]. The resulting porosity
 268 observed within the image (41%) matched well with the inferred porosity of the 30μm x 30μm
 269 x 30μm region initially identified from the macroscopic 10μm voxel size image of the 10mm
 270 diameter core. Stokes flow was simulated within this pore geometry using the LIR FlowDict
 271 solver [36] (Math2Market GeoDict), giving a nano-porous permeability of $2.63 \times 10^{-15} \text{ m}^2$.
 272

273 MICP was also simulated on this structure using the SatuDict modules of GeoDict
 274 (Math2Market), showing a good match in peak position between the microporous peak in the
 275 experimental MICP and the simulated MICP through the microporous structure [Figure 4].
 276



277
 278 **Figure 4** The real nano-XRM (solid black), real micro-CT (solid brown), synthetic (red and
 279 rainbow), and bulk core measured (black dashed) MICP curves.

280
 281 To extend this result to cover the porosity range observed within the microporosity a suite of
 282 similar pore networks were constructed using object based techniques [37]. The connected
 283 micritic matrix was separated into a network of discrete, separated micrite grains using a
 284 watershed algorithm [Figure 3E]. The volume and equivalent radius distribution of these grains
 285 was then measured, showing a unimodal distribution with a peak equivalent grain radius of
 286 around 500 nm [Figure 5].
 287



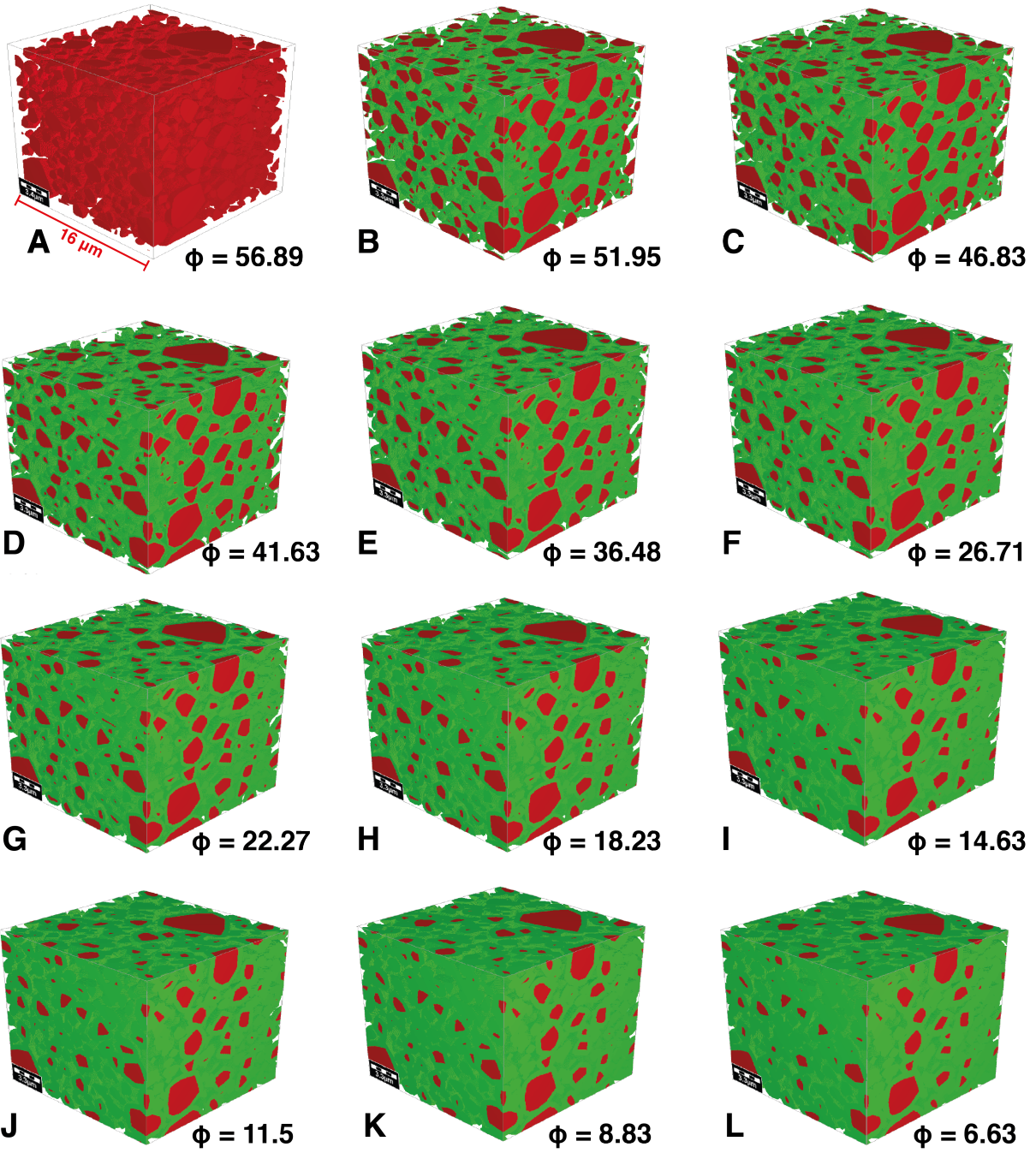
288

289
290
291
292
293
294
295
296
297
298
299
300
301
302
303
304
305
306
307
308
309
310
311

Figure 5 Micrite grain equivalent radii frequency histograms for the real geometry imaged by nano CT (black) and the 41% porosity synthetic image (red).

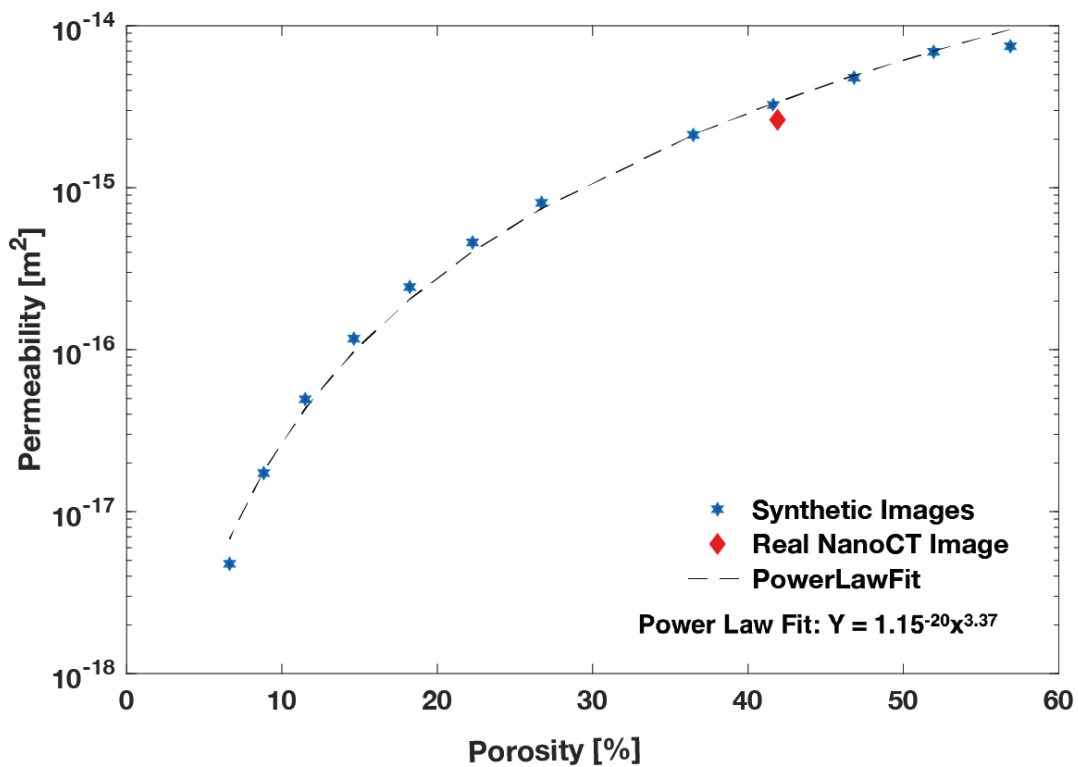
A histogram of the volumes of the separated grains and the porosity and permeability of the nano-XRM image is then used to generate synthetic grains in a pore space [Figure 6A]. All geometry creation was performed in GeoDict software using the GrainGeo module. These grains are then dilated successively to create twelve synthetic pore spaces with porosities ranging from 6.63 to 56.89.

A suite of pore geometries were then created by modelling the micritic grains as convex polyhedra, bounded by spheres with a radius distribution given by the radius distribution of the micritic grains. The polyhedra were placed randomly within a 3D volume of size $16 \times 16 \times 16 \mu\text{m}^3$ without allowing granular overlap until no more polyhedra could be fit within the pore geometry. This structure was then progressively dilated by 1 voxel at a time, with simulations of both MICP and Stokes-flow permeability performed on each successive pore network until no connected pore network remained [Figure 6B-L], creating a porosity-permeability relationship for the intragranular micritic micro-porosity in this sample [Figure 7]. We found that the porosity-permeability relationship corresponded to a power law fit with an exponent of 3.37 which is reasonable when compared to previous published Kozeny-Carmen estimations for porous rocks [38].



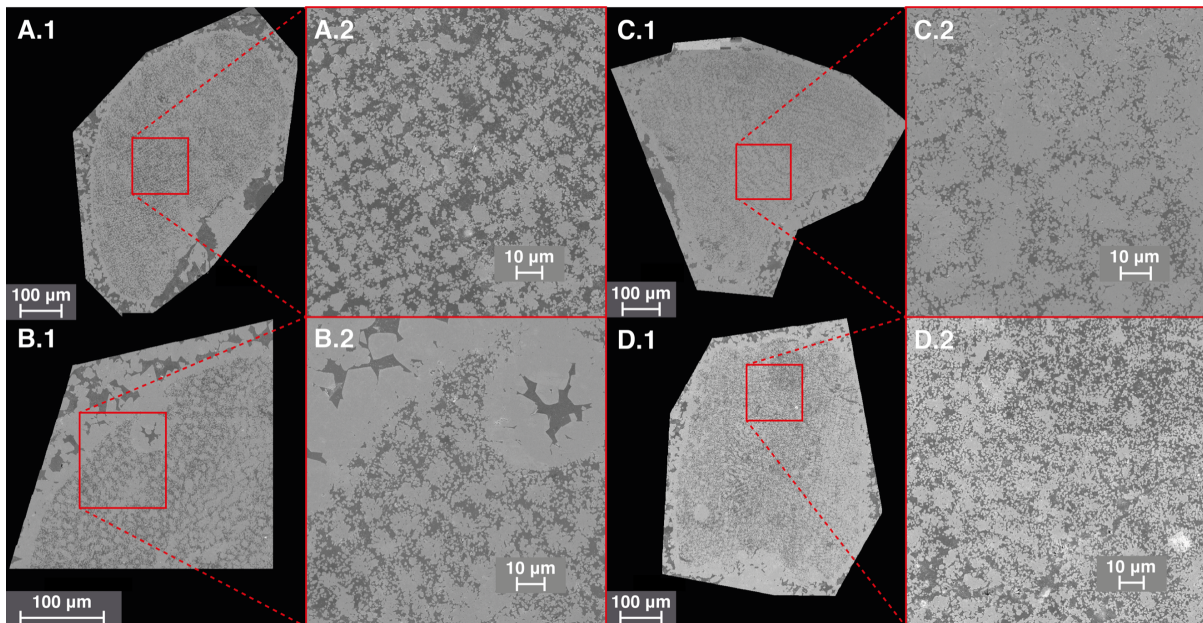
312
 313
 314
 315
 316
 317

Figure 6 (A) is the synthetic porespace generated from the volumetric grain size distribution from the nano-XRM image. (B-L) Dilated grains (green) with preserved grains (red) and pore space (clear).



318
 319 **Figure 7** The synthetic porosity-permeability relationship (blue stars), with the power law fit
 320 of $Y = 10^{-20}x^{3.72}$ (black dashes) and the real image porosity and permeability value (red
 321 diamond).

322
 323 In addition to nano-XRM imaging we also imaged several microporous grains using a Zeiss
 324 Sigma 300 SEM at a pixel resolution of 20 nm to examine the structural heterogeneity inside a
 325 microporous grain [Figure 8]. We found that the micritic structures were reasonably regular
 326 and consistent with our generated synthetic grain packings. However, it is interesting to note
 327 the high-density layers of compacted calcite on the outside of the grains which is likely to be
 328 lower permeability than the interior of the grains.
 329



330

331

332

333

334

335

336

337

338

339

340

341

342

343

344

345

346

347

348

349

350

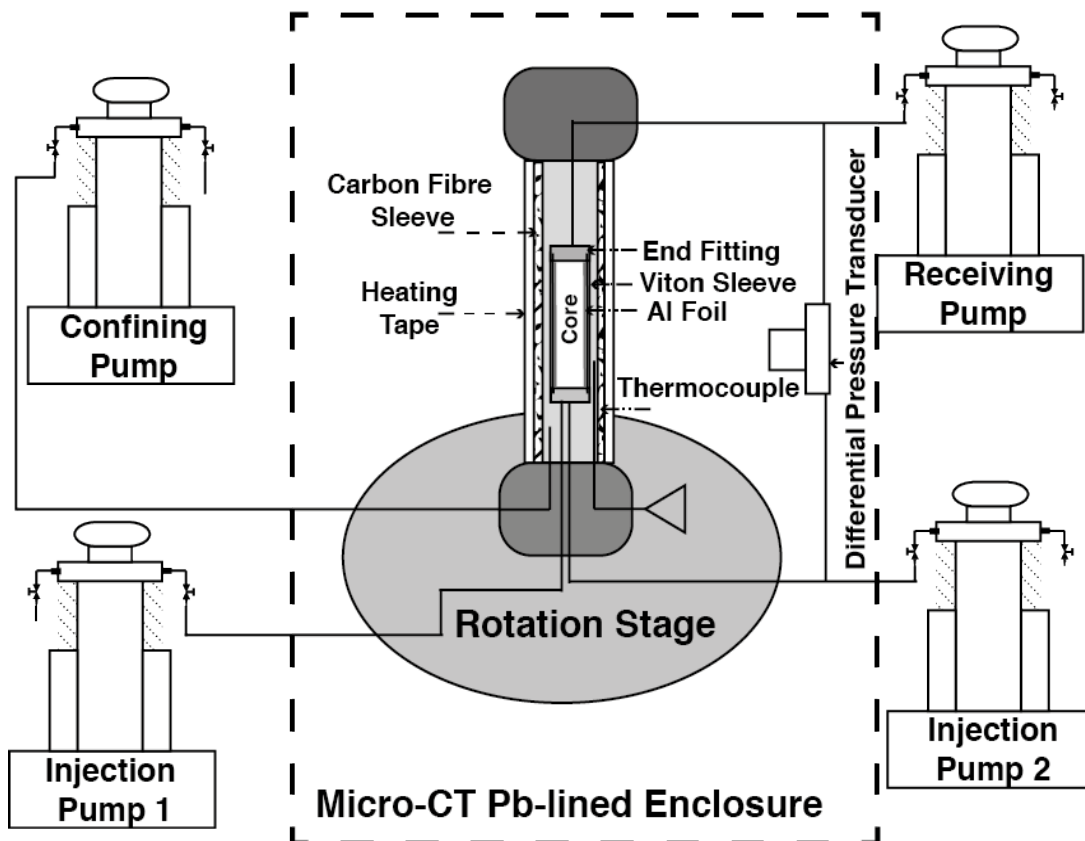
351

Figure 8 Estailades grains (A.1-D.1) and high-resolution sections (A.2-D.2) showing micritic calcite with some dense calcite around the grain boundaries.

Pore-scale experiments and imaging

A new 5mm diameter, 24mm long core of Estailades was then drilled from the same 1 m³ block of limestone as used for the nano scale study. The core was loaded into a carbon fibre core holder (airborne composites) and then imaged dry [Figure 11A]. The core was confined using DI water at 10 bar and two high pressure syringe (Teledyne isco) pumps were used to drive highly doped brine of 30 wt.% KI through the core with a constant back pressure of 2 bar [Figure 9] for 1000 pore volumes and reimaged with the brine inside. The core was washed with DI water for 1000 pore volumes and three differential pressure measurements were made using a Keller PD-33X differential pressure transducer with a total range of 300kbar and an error of 0.01% across the whole range during flow of 0.5 0.75 and 1.25 mL.min⁻¹ with a 2-bar back pressure [Figure 12A].

The core was then confined at 120 bar, the internal pore pressure raised to 100 bar and the temperature raised to 50°C. Nitrogen gas (N₂) was co-injected through the core with 30 wt. % KI brine and allowed to come to steady-state. The differential pressure was measured, and images of the core were taken *in situ*. Precise details of this experimental apparatus and method of measuring relative permeability can be found in [39].

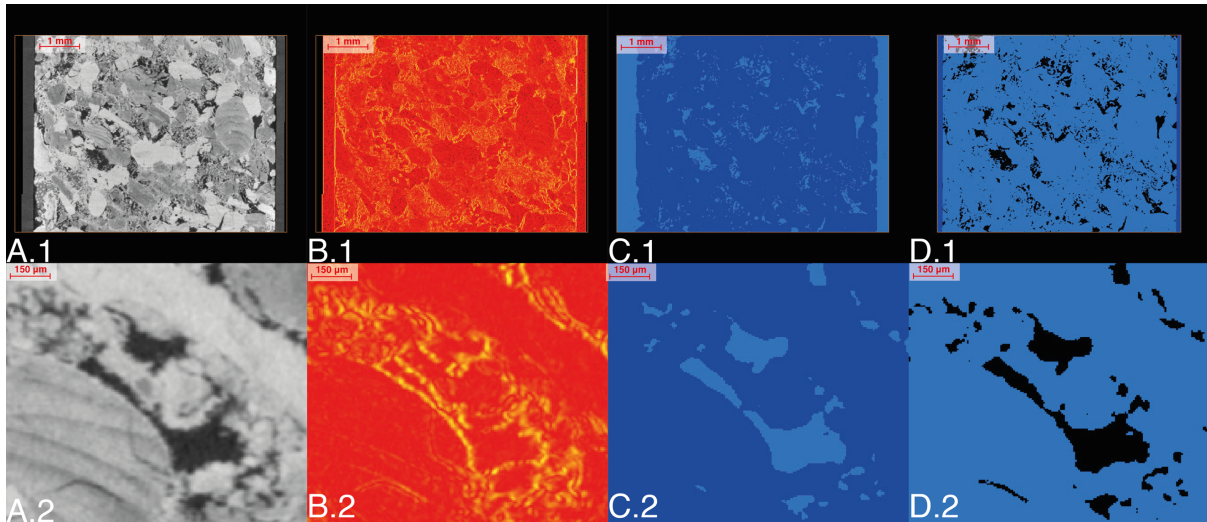


352
 353 **Figure 9** The experimental apparatus consists of the injection, receiving, and confining pumps
 354 outside the micro-CT, with a core holder and differential transducer on the rotation stage inside
 355 the micro-CT lead-lined enclosure. The core holder is made of carbon fibre and is equipped
 356 with thermocouples and heating wrap. The core is wrapped in Aluminium foil inside a viton
 357 sleeve which is attached to the end fittings supporting the two injection pumps and receiving
 358 pump.

359
 360 **Pore scale image processing**

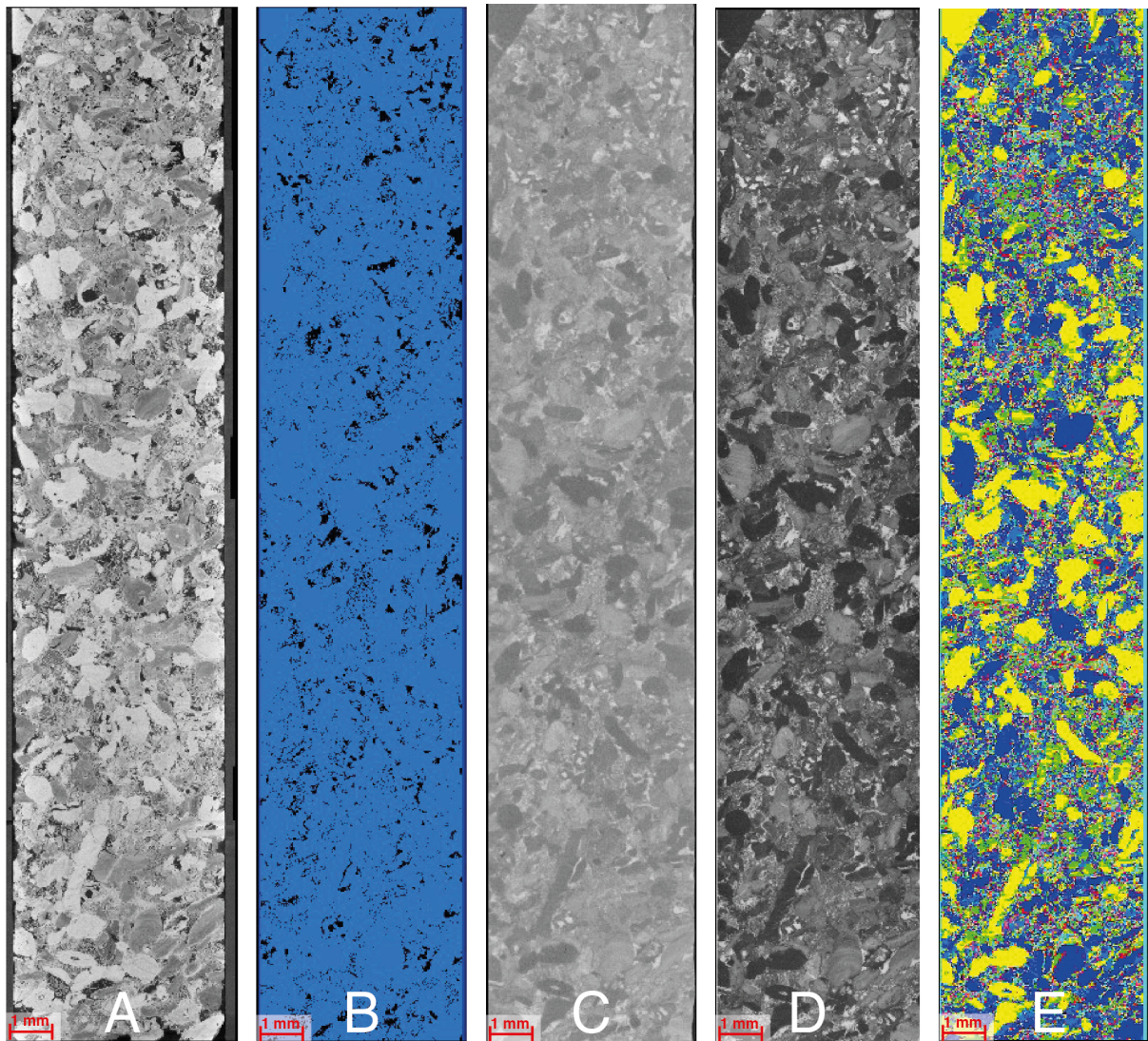
361
 362 Initially a watershed segmentation was performed on the dry image Estailades to identify
 363 regions of pore and rock [Figure 10]. While watershed segmentation gave a reasonable
 364 estimation of porosity and visual examination confirmed fidelity of pores, the pore space itself
 365 was unconnected across the length of the domain [Figure 10C]. Without a connected pore
 366 space, Stokes simulations are not possible. The reason for this dysconnectivity is inherent in
 367 the design of the watershed method where the tightest pore throats are most likely to suffer
 368 from partial volume effects and have smaller gradients in the gradient image [Figure 10B].
 369 These smaller gradients are less likely to be identified as pore space and thus the pore throats
 370 may be closed artificially. To combat this problem of closed throats we instead used machine
 371 learning segmentation which uses not only image gradients but texture and other higher order
 372 features to identify phases [Figure 10C]. It is important to note that while segmentation using
 373 machine learning can be more accurate, it takes longer to train the algorithm and is more
 374 computationally expensive compared to watershed [40, 41].

375



376
 377 **Figure 10** Watershed segmentation vs Weka 3D. The dry scan (A), gradient image (B),
 378 watershed segmentation (C), and Weka 3D machine learning segmentation (D) are shown at
 379 low (1) and high zoom (2).
 380

381 The Weka3D machine learning segmentation algorithm in Fiji was used to segment the macro
 382 pore space for both the Stokes and Stokes-Brinkman simulations [Figure 11B]. The images of
 383 the rock filled with doped brine were then used to identify the solid grains and unconnected
 384 micro-porosity. The pore space, unconnected micro-porosity and solid grains were then
 385 masked and the remaining greyscale values were used to label the connected microporous
 386 grains based on porosity using Avizo 9.3 (www.fei.com) [Figure 11D]. These porosities were
 387 then assigned a permeability based in FlowDict based on the permeability calculated on the
 388 synthetic pore spaces [Table 1]. A similar workflow was followed for the images of imaged *in*
 389 *situ* fluid distributions, with the images registered to the dry scan and then the nitrogen was
 390 segmented inside the pore space using a watershed algorithm on the difference image. The non-
 391 wetting phase saturation can then be calculated based on the number of pore-space voxels filled
 392 with gas. Figure 14 shows the nitrogen in the pore space visualised as small, medium, and large
 393 clusters.
 394
 395



396
397
398
399
400
401
402

Figure 11 The image processing workflow. The dry scan (A) is segmented using machine learning (B). The doped scan (C) is subtracted from the dry scan to get the difference image (D). The difference image greyscale is then thresholded to 12 different porosity values and grains and then the pore space of segmented dry scan (B) is masked to create the 14-phase segmentation of solid grains, 12 types of microporous grains, and pores (E).

403
404
405

Table 1 Porosity and permeability values for micro-porosity calculated from synthetic images.

Porosity Difference [%]	Range in Image	Porosity of Simulation [%]	Simulated Permeability [m^2]	Fraction of Total Core Volume [%]	Segmentation Phase #
100		N/A	N/A (Pore)	9.95	1
54.45 – 99.9		56.89	7.47×10^{-15}	17.16	2
49.4 – 54.4		51.95	6.91×10^{-15}	4.63	3
44.3 - 49.3		46.83	4.79×10^{-15}	4.62	4
39.1 - 44.2		41.63	3.24×10^{-15}	4.86	5
31.6 - 39.0		36.48	2.12×10^{-15}	7.22	6
24.5 – 31.5		26.71	8.06×10^{-16}	6.93	7
20.3 - 24.4		22.27	4.59×10^{-16}	4.09	8
16.5 - 20.2		18.23	2.44×10^{-16}	3.65	9
13.1 - 16.4		14.63	1.17×10^{-16}	3.21	10
10.2-13.0		11.5	4.95×10^{-17}	2.78	11
7.8-10.1		8.83	1.73×10^{-17}	2.36	12
0.1-7.7		6.63	4.76×10^{-18}	7.73	13
0		N/A	N/A (Grain)	20.83	14
N/A		N/A	0 (Viton Sleeve)	N/A	15

406
407
408

Numerical methods

409
410
411

All simulations in this paper were completed using modules contained in Math2Market GeoDict. This includes synthetic pore-space generation (GrainGeo), Stokes flow (FlowDict), Stokes-Brinkman flow (FlowDict), and synthetic MICP injection (SatuDict).

412

413
414
415
416
417

The GrainGeo module in GeoDict [42] can be used to create digital 3D models of ceramics, sintered materials, grain packings or digital rocks. The starting point for modelling are user-defined parameter such as known grain size distribution, pore size distribution and grain shapes. By changing the parameters of the underlying the model, new material structures are designed and their material properties can be studied.

418

419
420
421
422
423
424
425
426
427
428
429
430

The LIR solver [36] in the FlowDict module is a very fast and memory efficient iterative finite volume method. The solver computes the permeability, as well as velocity and pressure fields, on large 3D images. The LIR solver can be used for the numerical solution of the Stokes, Stokes-Brinkman, Navier-Stokes, and Navier-Stokes-Brinkman equations. Usually, 3D images are represented as regular voxel grids where the number of grid cells grows cubically. The LIR solver uses an adaptive grid, instead of a regular grid, to reduce significantly the number of grid cells. The basis of the adaptive grid is a data structure called LIR-tree [43] that is used for spatial partitioning of 3D images. The pore space is coarsened in areas with small velocity and pressure variations, while keeping the original resolution near the solid surfaces and in regions where velocity or pressure vary rapidly. Pressure and velocity are discretized on staggered grids and they are arranged in such a way that each cell can satisfy the (Navier-)Stokes(-Brinkman)-equations independently from its neighbour cells.

431

432
433

The pore morphology method [44] is used in SatuDict and it predicts the distribution of a wetting phase (WP) and a non-wetting phase (NWP) inside a porous medium. The method

434 distributes two fluids by using morphological operations rather than solving partial differential
435 equations. For drainage, it can be envisioned that spheres are pushed into the structure and
436 placed in the pore space where the pore size is greater than a certain radius. The radius is
437 decreased in an iterative process and this corresponds to an increase of the capillary pressure.
438 The superposition of all spheres represents the NWP. The pore morphology method achieves
439 this placement of spheres by dilation and erosion processes of the solid phase with the pore
440 space. Additional connectivity checks [45] with respect to NWP and WP reservoirs can be used
441 to increase the validity of the distributions and they allow to introduce residual phases. The
442 output of the algorithm is a finite sequence of quasi-stationary states. For relative permeability
443 of the WP, for instance, we solve a single-phase flow inside the WP and treat the interface
444 between WP and NWP as immobile no-slip interface.

445

446 RESULTS AND DISCUSSION

447

448 Differential pressure measurements were used with Darcy's Law:

449

450

$$k = - \frac{Q\mu L}{A(\Delta P)}$$

451

452 where k is permeability [m^2], Q is the flowrate [$\text{m}^3 \cdot \text{s}^{-1}$], μ is viscosity [$\text{mPa} \cdot \text{s}^{-1}$], L is the length
453 of the core [m], A is the cross-sectional area of the core [m^2], and ΔP [Pa] is the differential
454 pressure between the inlet and the outlet of the core. The calculated permeability from the
455 differential pressure measurements was $2.43 \times 10^{-14} \text{ m}^2$ [Figure 12A]. Each of the large-scale
456 simulations were run for 162 hours on 24 3.0GHz cores. The Stokes simulation used around
457 80 GB of RAM while the Stokes-Brinkman used around 256 GB of RAM. Unfortunately, due
458 to memory constraints, the least permeable phases (1-5) were set to zero permeability in the
459 Stokes-Brinkman simulations. The estimated permeability of the Stokes simulation was $1.21 \times$
460 10^{-14} m^2 while the Stokes-Brinkman simulation was $3.57 \times 10^{-14} \text{ m}^2$. These values indicate that
461 the Stokes simulation underestimated permeability by 50% while the Stokes-Brinkman
462 simulation overestimated permeability by 46%.

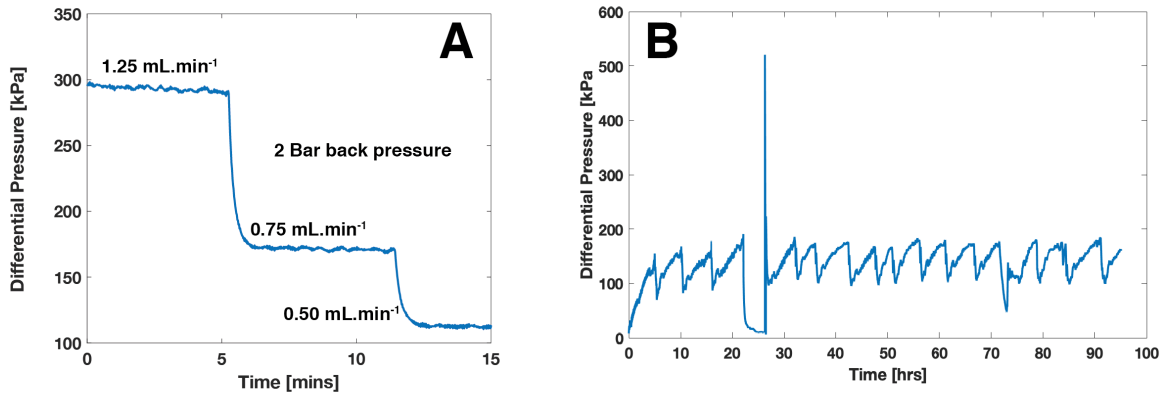
463

464 There are two likely sources of error in the Stokes simulations – segmentation error and
465 unaccounted-for contributions of micro-porosity to permeability. It is possible that the Weka
466 segmentation needs more training and is still not capturing all of the small pore throats that
467 contribute to flow. However, we believe that it is more likely the lack of microporous regions
468 that closes off flow in places that would otherwise have hydraulic connection as we see in the
469 high-density calcite crystal layer on the SEM images of exterior of the grains in Figure 8.

469

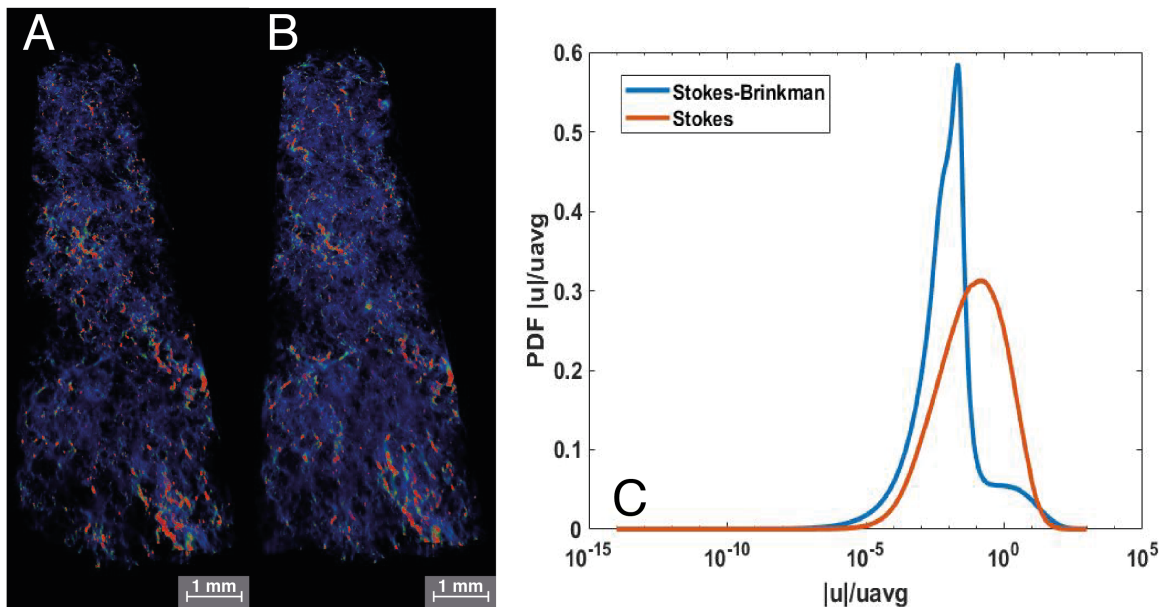
470 In contrast, the Stokes-Brinkman simulation overpredicts permeability. We posit this could
471 be due to an overprediction of connectivity in the microporous regions which is also consistent
472 with Figure 8. While our method of doped brine flooding should minimise misidentification of
473 completely unconnected areas of micro porosity, if there is a minor hydraulic connection the
474 doped brine would still flood the area very slowly and by the time 100 pore volumes have been
475 flooded through the core the micro-porosity would be completely flooded. A possible solution
476 to this problem would be to do time-resolved imaging during doped brine flooding to have
477 some idea of the local connectivity of each microporous voxel.

477



478
 479 **Figure 12** (A) Differential pressure [kPa] measurements across the core at brine flowrates of
 480 1.25, 0.75, and 0.5 mL.min⁻¹ with a back pressure of 2 Bar. (B) Differential pressure measured
 481 during co-injection of N₂ and KI brine.
 482

483 The velocity fields and probability density functions (PDFs) of velocity are shown in
 484 Figure 13. A visual inspection of the velocity fields does not reveal very much difference.
 485 However, when we compare the PDFs of velocity in Figure 13C we see a distinct difference in
 486 the peak velocities and tail. In the Stokes simulation the velocity PDF is a smooth gaussian
 487 distribution with a peak centred around 1. However, in the Stokes-Brinkman simulation we see
 488 a smaller secondary peak around 1 with the main peak around 10⁻² with a long tail. This
 489 indicates that in the Stokes simulation we are only capturing advective flow while in the Stokes-
 490 Brinkman simulation there is a large amount of slow flow through the micro pore space. This
 491 result has many applications but is particularly important during contaminant transport for
 492 predicting the concentration of contaminants with time. If the slower transport is not
 493 incorporated into the model than the peak and the tail will not be accurately predicted.
 494



495
 496 **Figure 13** Velocity fields rendered with high velocities in red and low velocities in blue for
 497 Stokes (A) and Stokes-Brinkman Simulations (B). The PDF's of velocity (C) are shown for
 498 Stokes (red) and Stokes Brinkman (blue) simulations.
 499
 500

501 The segmentation technique employed for the macro pore space may also have a significant
502 control on the simulated velocity PDF. As discussed in the methods section, when a typical
503 watershed segmentation was attempted on this image the macro pore space was unconnected
504 throughout the length of the samples. In previous studies watershed has been used to segment
505 the pore space and the predicted permeability values were far below the ones predicted in this
506 paper. Menke, Bijeljic [46], Menke, Andrew [47], Menke, Bijeljic [48] report values ranging
507 from 1.53×10^{-14} to $1.57 \times 10^{-13} \text{ m}^2$. It is likely that pore space remained connected in these
508 cases because while the samples were imaged at approximately the same resolution, they were
509 significantly shorter (and thus overall contained less heterogeneity). However, the watershed
510 segmentation still did not properly segment the small throats and thus the permeability was
511 predicted to be much lower than would be expected from the bulk measured permeability of
512 $1.490 \times 10^{-12} \text{ m}^2$. For complex pore structures watershed segmentation will be less accurate as
513 the more sophisticated textural and featural segmentation approaches and should be used with
514 caution.

515

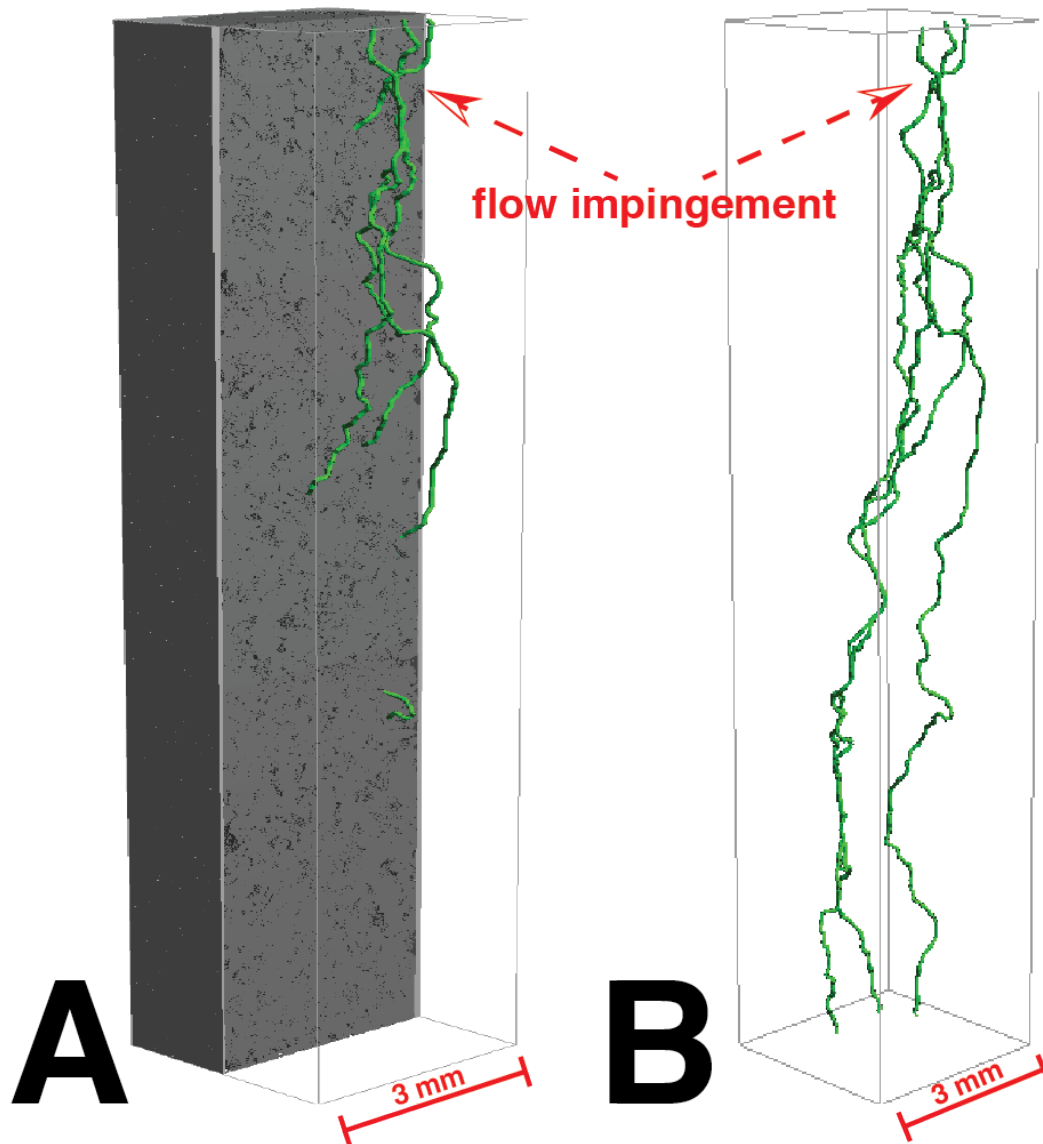
516 During co-injection we measured differential pressure for 95 hours. We observed a cyclic
517 perturbation where pressure builds from $\sim 90 \text{ kPa}$ to $\sim 180 \text{ kPa}$ over the course of ~ 5 hours and
518 then suddenly drops back down. These pressures correspond to wetting phase permeabilities
519 fluctuating between $1.52 \times 10^{-15} \text{ m}^2$ and $2.74 \times 10^{-15} \text{ m}^2$. We imaged the core during flow and
520 observed that the non-wetting phase saturation to be 0.6 in the macro pore space. It is important
521 to note that as each scan took around 5 hours any changes in saturation during this period would
522 be time-averaged. To try and understand why the pressure was building and releasing we
523 modelled the streamlines through the core using FlowDict [Figure 15]. We found that all flow
524 of the non-wetting phase is directed through a single small pore throat about two thirds of the
525 way through the core. We postulate that this small flow impedance was causing capillary
526 pressure to build and then be released as the local capillary pressure built enough to flow
527 through this small pore throat, a theory supported by the approximately periodic nature of the
528 pressure fluctuations [49, 50]. More experiments targeting the investigation of this theory
529 would be an interesting target for future research, however, are out of the scope of this paper.

530

531 Relative permeability was then simulated by simulating fluid distributions using SatuDict,
532 injecting non-wetting phase into the core from both sides using a maxima-inscribed-spheres
533 technique on the connected pore network, slowly increasing the saturation from 0 to 1.
534 Permeability was calculated by simulating flow through the wetting-phase as a single-phase
535 permeability using both Stokes and Stokes-Brinkman methods. We found that initially the
536 permeability estimation ranged between 1.21×10^{-14} and $1.14 \times 10^{-14} \text{ m}^2$ for non-wetting phase
537 saturation of 0 to 0.036, but that after this saturation the non-wetting phase completely blocks
538 all connected pathways and the permeability is predicted as zero. In the Stokes-Brinkman
539 simulations, however, we observe that the initial permeabilities are higher than the Stokes flow
540 with values ranging from 3.57×10^{-14} to $2.92 \times 10^{-14} \text{ m}^2$ for non-wetting phase saturation of 0
541 to 0.067. Furthermore, there is a connected flow path for all saturations, and we find that the
542 predicted permeability of $2.30 \times 10^{-15} \text{ m}^2$ at a saturation of 0.59 is in good agreement with the
543 experimental measurements.

544

545



554
 555 **Figure 15** The three widest percolation paths through the core shown in green with the rock
 556 shown in grey (A) and the rock transparent (B).

557
 558 CONCLUSIONS

559
 560 We have developed a method of using multiscale imaging and experiments to characterize
 561 relative permeability in a microporous carbonate, even at high non-wetting phase saturations.
 562 Intra-granular micro-porosity in this system was characterized using targeted nano X-ray
 563 microscopy, which was then used to generate a suite of synthetic pore geometries
 564 hydrodynamically similar to the imaged network. This was used to generate a customized
 565 Kozeny-Carman porosity-permeability relationship which was used to populate a macroscopic
 566 porosity map, generated from the (macro-scale) X-ray microscopy.

567
 568 By coupling multi-phase flow simulation with a multi-scale description of flow we were
 569 accurately able to predict relative permeability at a fractional flow of 0.5, where a single-scale
 570 simulation failed to capture an effective flow pathway - the wetting phase disconnected in the
 571 macro-pore space, only remaining connected through the micro-porosity. Such a multiscale
 572 approach is particularly powerful when attempting to assess systems with high levels of

573 multiscale structural heterogeneity, such as complex carbonate and shale reservoirs. It also
574 shows that, while these systems can be extremely challenging to characterize, they are tractable
575 by coupling state-of-the-art imaging technologies with stochastic network generation, guided
576 by a geological understanding of the medium in question.

577

578 Future work may include the extension of these analyses across the full experimental relative
579 permeability curve, fast tomography imaging to observe dynamic changes in saturation, further
580 (quantitative) assessment and comparison of micritic structures across several rock types.

581

582 ACKNOWLEDGEMENTS

583

584 We gratefully acknowledge funding from the Qatar Carbonates and Carbon Storage Research
585 Centre (QCCSRC), provided jointly by Qatar Petroleum, Shell, and the Qatar Science &
586 Technology Park. We thank Professor Martin Blunt for his support in this research.

587

588 REFERENCES

589

590 [1] Blunt MJ, B Bijeljic, H Dong, O Gharbi, S Iglauer, P Mostaghimi, et al. Pore-scale imaging
591 and modelling. *Advances in Water Resources*. 51 (2013) 197-216.

592 [2] Noiriel C. Resolving time-dependent evolution of pore-scale structure, permeability and
593 reactivity using X-ray microtomography. *Rev Mineral Geochem*. 80 (2015) 247-85.

594 [3] Blunt MJ. *Multiphase flow in permeable media: A pore-scale perspective*. Cambridge
595 University Press, 2017.

596 [4] Lai P, K Moulton, S Krevor. Pore-scale heterogeneity in the mineral distribution and
597 reactive surface area of porous rocks. *Chemical Geology*. 411 (2015) 260-73, doi:
598 10.1016/j.chemgeo.2015.07.010.

599 [5] McClure JE, RT Armstrong, MA Berrill, S Schlüter, S Berg, WG Gray, et al. A geometric state
600 function for two-fluid flow in porous media. arXiv preprint arXiv:180511032. (2018).

601 [6] Armstrong RT, JE McClure, MA Berrill, M Rücker, S Schlüter, S Berg. Beyond Darcy's law:
602 The role of phase topology and ganglion dynamics for two-fluid flow. *Physical Review E*. 94
603 (2016) 043113.

604 [7] Mostaghimi P, MJ Blunt, B Bijeljic. Computations of absolute permeability on micro-CT
605 images. *Mathematical Geosciences*. 45 (2013) 103-25.

606 [8] Alyafei N, AQ Raeini, A Paluszny, MJ Blunt. A sensitivity study of the effect of image
607 resolution on predicted petrophysical properties. *Transport in Porous Media*. 110 (2015) 157-
608 69.

609 [9] Al-Ansi N, O Gharbi, AQ Raeini, J Yang, S Iglauer, MJ Blunt. Influence of micro-computed
610 tomography image resolution on the predictions of petrophysical properties. IPTC 2013:
611 International Petroleum Technology Conference 2013.

612 [10] Choquette PW, LC Pray. Geologic nomenclature and classification of porosity in
613 sedimentary carbonates. *AAPG bulletin*. 54 (1970) 207-50.

614 [11] Archie GE. Classification of carbonate reservoir rocks and petrophysical considerations.
615 *AAPG Bulletin*. 36 (1952) 278-98.

616 [12] Schlumberger. *Carbonate Reservoirs: Meeting unique challenges to maximize recovery*.
617 2007.

618 [13] Neale G, W Nader. Practical significance of Brinkman's extension of Darcy's law: coupled
619 parallel flows within a channel and a bounding porous medium. *The Canadian Journal of*
620 *Chemical Engineering*. 52 (1974) 475-8.

621 [14] Beavers GS, DD Joseph. Boundary conditions at a naturally permeable wall. *Journal of*
622 *fluid mechanics.* 30 (1967) 197-207.

623 [15] Taud H, R Martinez-Angeles, J Parrot, L Hernandez-Escobedo. Porosity estimation
624 method by X-ray computed tomography. *Journal of petroleum science and engineering.* 47
625 (2005) 209-17.

626 [16] Carman P. Fluid flow through granular beds. *Transactions-Institution of Chemical*
627 *Engineeres.* 15 (1937) 150-66.

628 [17] Carman PC. Permeability of saturated sands, soils and clays. *The Journal of Agricultural*
629 *Science.* 29 (1939) 262-73.

630 [18] Soulaire C, HA Tchepeli. Micro-continuum approach for pore-scale simulation of
631 subsurface processes. *Transport in Porous Media.* 113 (2016) 431-56.

632 [19] Lin Q, Y Al-Khulaifi, MJ Blunt, B Bijeljic. Quantification of sub-resolution porosity in
633 carbonate rocks by applying high-salinity contrast brine using X-ray microtomography
634 differential imaging. *Advances in water resources.* 96 (2016) 306-22.

635 [20] Ott H, M Andrew, J Snippe, MJ Blunt. Microscale solute transport and precipitation in
636 complex rock during drying. *Geophysical Research Letters.* 41 (2014) 8369-76.

637 [21] Wargo E, T Kotaka, Y Tabuchi, E Kumbur. Comparison of focused ion beam versus nano-
638 scale X-ray computed tomography for resolving 3-D microstructures of porous fuel cell
639 materials. *Journal of Power Sources.* 241 (2013) 608-18.

640 [22] Hlawacek G, V Veligura, R van Gastel, B Poelsema. Helium ion microscopy. *Journal of*
641 *Vacuum Science & Technology B, Nanotechnology and Microelectronics: Materials,*
642 *Processing, Measurement, and Phenomena.* 32 (2014) 020801.

643 [23] Scipioni L, L Stern, J Notte, S Sijbrandij, B Griffin. Helium ion microscope. *Advanced*
644 *Materials and Processes.* 166 (2008) 27.

645 [24] Bear J. *Dynamics of Fluids in Porous Media.* Courier Dover Publications, 1972.

646 [25] Singh K, H Scholl, M Brinkmann, M Di Michiel, M Scheel, S Herminghaus, et al. The role
647 of local instabilities in fluid invasion into permeable media. *Scientific reports.* 7 (2017) 444.

648 [26] Phenrat T, H-J Kim, F Fagerlund, T Illangasekare, RD Tilton, GV Lowry. Particle size
649 distribution, concentration, and magnetic attraction affect transport of polymer-modified FeO
650 nanoparticles in sand columns. *Environmental science & technology.* 43 (2009) 5079-85.

651 [27] Tohidi B, R Anderson, MB Clennell, RW Burgass, AB Biderkab. Visual observation of gas-
652 hydrate formation and dissociation in synthetic porous media by means of glass micromodels.
653 *Geology.* 29 (2001) 867-70.

654 [28] Zuo L, CY Zhang, RW Falta, SM Benson. Micromodel investigations of CO₂ exsolution from
655 carbonated water in sedimentary rocks. *Advances in Water Resources.* 53 (2013) 188-97, doi:
656 10.1016/j.advwatres.2012.11.004.

657 [29] Okabe H, MJ Blunt. Pore space reconstruction using multiple-point statistics. *Journal of*
658 *Petroleum Science and Engineering.* 46 (2005) 121-37.

659 [30] Andrew M. Comparing organic hosted and intergranular pore networks: Topography
660 and Topology in Grains, Gaps & Bubbles. In Review. (2018).

661 [31] Linden S, T Cvjetkovic, E Glatt, A Wiegmann. An integrated approach to compute physical
662 properties of core samples. *Proceedings of SCA Avignon.* (2014).

663 [32] Roth S, Y Hong, H Bale, T Zhao, S Bhattiprolu, M Andrew, et al. Fully controlled sampling
664 workflow for multi-scale X-ray imaging of complex reservoir rock samples to be used for
665 digital rock physics. *Search and Discovery.* (2016).

666 [33] Andrew M. *Reservoir-Condition Pore-Scale Imaging of Multiphase Flow.* London: Imperial
667 College London; 2015.

668 [34] Berg S, N Saxena, M Shaik, C Pradhan. Generation of ground truth images to validate
669 micro-CT image-processing pipelines. *The Leading Edge*. 37 (2018) 412-20.

670 [35] Andrew M, B Hornberger. Benchmarking of Machine Learning and Conventional Image
671 Segmentation Techniques on 3D X-ray Microscopy Data. *Microscopy and Microanalysis*. 24
672 (2018) 120-1.

673 [36] Linden S, A Wiegmann, H Hagen. The LIR space partitioning system applied to the Stokes
674 equations. *Graphical Models*. 82 (2015) 58-66, doi: 10.1016/j.gmod.2015.06.003.

675 [37] Andrew M. Comparing organic-hosted and intergranular pore networks: topography and
676 topology in grains, gaps and bubbles. Geological Society, London, Special Publications. 484
677 (2018) SP484. 4.

678 [38] Pape H, C Clauser, J Iffland. Variation of permeability with porosity in sandstone
679 diagenesis interpreted with a fractal pore space model. *Fractals and dynamic systems in
680 geoscience*. Springer2000. pp. 603-19.

681 [39] Gao Y, Q Lin, B Bijeljic, MJ Blunt. X-ray microtomography of intermittency in multiphase
682 flow at steady state using a differential imaging method. *Water Resources Research*. 53
683 (2017) 10274-92.

684 [40] Arganda-Carreras I, V Kaynig, C Rueden, KW Eliceiri, J Schindelin, A Cardona, et al.
685 Trainable Weka Segmentation: a machine learning tool for microscopy pixel classification.
686 *Bioinformatics*. 33 (2017) 2424-6.

687 [41] Arganda-Carreras I, V Kaynig, J Schindelin, A Cardona, H Seung. Trainable Weka
688 segmentation: a machine learning tool for microscopy image segmentation. *Neuroscience*.
689 2014 (2014) 73-80.

690 [42] S. L, C L., W A. Specialized methods for direct numerical simulations in porous media.
691 Kaiserlautern, Germany, 2018.

692 [43] Linden S, H Hagen, A Wiegmann. The LIR space partitioning system applied to Cartesian
693 grids. *International Conference on Mathematical Methods for Curves and Surfaces*.
694 Springer2012. pp. 324-40.

695 [44] Hilpert M, CT Miller. Pore-morphology-based simulation of drainage in totally wetting
696 porous media. *Advances in Water Resources*. 24 (2001) 243-55.

697 [45] Ahrenholz B, J Tölke, P Lehmann, A Peters, A Kaestner, M Krafczyk, et al. Prediction of
698 capillary hysteresis in a porous material using lattice-Boltzmann methods and comparison to
699 experimental data and a morphological pore network model. *Advances in Water Resources*.
700 31 (2008) 1151-73.

701 [46] Menke HP, B Bijeljic, MG Andrew, MJ Blunt. Dynamic Three-Dimensional Pore-Scale
702 Imaging of Reaction in a Carbonate at Reservoir Conditions. *Environmental Science &
703 Technology*. 49 (2015) 4407-14, doi: 10.1021/es505789f.

704 [47] Menke HP, MG Andrew, MJ Blunt, B Bijeljic. Reservoir Condition Imaging of Reactive
705 Transport in Heterogeneous Carbonates Using Fast Synchrotron Tomography – Effect of Initial
706 Pore structure and Flow Conditions. *Chemical Geology*. 428 (2016) 15-26, doi:
707 10.1016/j.chemgeo.2016.02.030.

708 [48] Menke H, B Bijeljic, M Blunt. Dynamic Reservoir-Condition Microtomography of Reactive
709 Transport in Complex Carbonates: Effect of Initial Pore Structure and Initial Brine pH.
710 *Geochimica et Cosmochimica Acta*. 204 (2017) 267-85, doi: 10.1016/j.gca.2017.01.053.

711 [49] Reynolds CA, H Menke, M Andrew, MJ Blunt, S Krevor. Dynamic fluid connectivity during
712 steady-state multiphase flow in a sandstone. *Proceedings of the National Academy of
713 Sciences*. 114 (2017) 8187-92.

714 [50] Spurin C, T Bultreys, B Bijeljic, MJ Blunt, S Krevor. Intermittent pathways in steady-state
715 two-phase flow: controlling mechanisms and impact on connectivity. Nature
716 Communications. IN REVIEW (2019).
717